



Semnan University

Mechanics of Advanced Composite Structures

Journal homepage: <https://macs.semnan.ac.ir/>

ISSN: 2423-7043



Research Article

Vibration Analysis of Sandwich Beams with Magnetorheological Elastomer Core and FGM Graphene Nanoplatelet-Reinforced Polymer Faces on Viscoelastic Foundation

Mohammad Javad Arabloo Faraji ^a , Ali Ghorbanpour Arani ^{a*} ,
Ehsan Mamnoun ^a , Zahra Khoddami Maraghi ^b

^a Department of Solid Mechanics, Faculty of Mechanical Engineering, University of Kashan, Kashan, Iran

^b Faculty of Engineering, Mahallat Institute of Higher Education, Mahallat, Iran

ARTICLE INFO

ABSTRACT

Article history:

Received: 2024-07-08

Revised: 2024-12-31

Accepted: 2025-02-02

Keywords:

Free vibration;
Sandwich beam;
Magnetorheological elastomer;
Graphene nanoplatelet-reinforced polymer;
Viscoelastic foundation.

This study investigates the free vibrations of a sandwich beam with a magneto-rheological elastomer (MRE) core reinforced with carbon nanotubes (CNTs) and polymer facings reinforced with graphene nanoplatelets (GNPs) resting on a viscoelastic foundation. To enhance the accuracy of the results, the modeling of the core and facings of the beam is based on the Timoshenko beam model, and the viscoelastic foundation is based on the visco-Pasternack model. The governing equations and boundary conditions are derived using Hamilton's principle and solved using Navier's method. After validation, the effects of beam parameters, including the applied magnetic field intensity, core and facing thicknesses, volume fraction of CNTs added to the core, volume fraction and distribution pattern of GNPs added to the facings, and foundation parameters, on the natural frequencies of the beam in different vibration modes are investigated. The results show that if the goal is to maximize the natural frequencies of the beam, adding GNPs to the polymer facings of the beam is significantly more effective than adding CNTs to the MRE core or increasing the applied magnetic field intensity to the core. The results of this research can be used in the design of sensors and actuators in many industries.

© 2025 The Author(s). Mechanics of Advanced Composite Structures published by Semnan University Press.

This is an open-access article under the CC-BY 4.0 license. (<https://creativecommons.org/licenses/by/4.0/>)

1. Introduction

The expected properties of a sandwich structure after construction. The first factor encompasses each material's intrinsic characteristics and properties, including thermal, mechanical, and electrical properties, which are inherently fixed and specific for different materials. However, the second factor consists of the properties and characteristics that arise from the interaction between the materials when

placed together. In other words, when two materials are placed side by side, they impact each other's performance, and understanding this is crucial for designing such structures. Ultimately, a proper understanding of the mechanics of sandwich structures is necessary to select suitable materials for the core and surfaces. Expected properties of a sandwich structure include high flexibility, strength-to-weight ratio, impact resistance, and thermal tolerance. Considering these properties, the

* Corresponding author.

E-mail address: aghorban@kashanu.ac.ir

Cite this article as:

Arabloo Faraji, M. J., Ghorbanpour Arani, A., Mamnoun, E. and Khoddami Maraghi, Z., 2025. Vibration Analysis of Sandwich Beams with Magnetorheological Elastomer Core and FGM Graphene Nanoplatelet-Reinforced Polymer Faces on Viscoelastic Foundation. *Mechanics of Advanced Composite Structures*, 12(3), pp. 447-464.

<https://doi.org/10.22075/MACS.2025.34687.1695>

sandwich structure enables the optimization of structures relative to the expected performance. Sandwich structures are beneficial for manufacturing components with weight constraints and critical weight considerations, such as parts of spacecraft, aircraft, and marine structures. Given the intriguing properties of fluids and MREs and their potential for vibration control in various structures, a group of researchers analyzed the mechanical behavior of sandwich structures with cores made of magneto-rheological materials. These articles can generally be classified into three categories: analytical articles, experimental articles, and analytical-experimental articles. The effect of a magnetic field on the vibrational behavior of an MRE sandwich micro-electromechanical system (MEMS) operating with electrostatic excitation and conductive layers was investigated by Akhavan et al. [1] using the method of multiple scales (MMS). To examine the vibrational behavior of the moving electrode, the Euler-Bernoulli beam theory, and Hamilton's principle were utilized to derive the equations. The results of this study indicate that by incorporating an MRE core in the moving electrode and applying various magnetic fields to it, the natural frequency of its vibration can be controlled. Specifically, the system's natural frequency increases with an increase in the applied magnetic field. The influence of various factors such as the electric potential difference between the two electrodes, changes in the core and layer thickness, and changes in the system's vibration modes on the natural frequencies were examined. A new hysteresis model based on the curve fitting method to represent the highly nonlinear and hysteretic relationships between shear force and displacement response of an MRE base isolator was proposed by Yu et al. [2]. Compared to classical hysteresis models such as the Bouc-Wen or LuGre friction models, the proposed model combines a hyperbolic sine function and a Gaussian function to model the hysteresis loops of the device's response, resulting in a significant reduction in the number of model parameters. Experimental results of the device under both harmonic and random excitations were used to validate the performance of the proposed hybrid model and parameter identification algorithm with satisfactory results. Numerical results show that the CNT-reinforced composite cylindrical multi-MRE sandwich shell has a significant effect on natural frequencies compared to the single MRE cylindrical sandwich shell. Using computational fluid dynamics (CFD) software and presenting a two-dimensional model, Gedik et al [3] simulated the mechanical behavior of a magneto-rheological fluid confined between two parallel

fixed plates and subjected to an external magnetic field. In this study, relying on the assumption of steady flow and the incompressibility of the magneto-rheological fluid, they investigated the effect of applying a uniform magnetic field on the pressure distribution and velocity changes of the fluid. Haghparast et al [4] investigated the influence of fluid-structure interaction (FSI) on the vibration of a moving sandwich plate with a balsa wood core and nanocomposite face sheets. This study presents a theoretical analysis of the vibrations of a vertically moving sandwich plate floating on a fluid. The plate consists of a balsa wood core and two nanocomposite face sheets, which vibrate as an integrated sandwich. The FSI effect on the stability of the moving plate is considered for both ideal and viscous fluid conditions. The results indicate that the dimensionless frequencies of the moving sandwich plate decrease rapidly with increasing water levels and become almost independent of the fluid level when it exceeds 50% of the plate length. Ghorbanpour Arani et al.[5] investigated the frequency response of a smart sandwich plate composed of magnetic face sheets and a nanofiber-reinforced core. The analysis employed the third-order shear deformation theory (Reddy's theory) and revealed insightful details regarding the influence of various parameters, including in-plane forces, elastic foundation modulus, core-to-face sheet thickness ratio, and velocity feedback gain controller on the dimensionless frequency of the sandwich plate. In another study, Zarastvand et al. [6] conducted a comprehensive review to gather, categorize, and organize all previous research on the sound insulation characteristics of plate structures from 1967 to the present. This review encompassed over 200 articles focused on the acoustic performance of these structures. All existing papers were classified and categorized based on relevant themes. In addition to providing appropriate descriptions of the topic's significance, fundamental equations, and general principles were developed in this area. Subsequently, the study delved into various theories to present reliable results based on the thickness of the structures. In another study, Ghafouri et al. [7] proposed an analytical approach to precisely investigate the impact of employing 3D re-entrant auxetic cellular structures (RACS) on the sound transmission loss (STL) of a sandwich panel. The dynamic equations governing fluid-structure interaction were derived using a 3D stress distribution, and the resulting equations were subsequently solved analytically using the state-space method. The reliability and accuracy of the obtained results were validated against previous studies.

Their findings indicated that the designed sandwich model significantly enhances the system's sound characteristics, as demonstrated by STL comparisons between the current approach and single-layer plates as well as sandwich panels with different core geometries. In another study, Zarastvand et al. [8] conducted a comprehensive review of the existing literature on sound transmission through multilayered plate structures. They compiled a comprehensive resource, reviewing and describing approximately 410 references from 1949 to 2020. In addition to providing a thorough explanation of the significance of acoustic analysis for these structures, the study also presents appropriate formulations. Furthermore, a review of related topics is conducted. Subsequently, the papers are categorized based on their acoustic excitation fields, including plane wave, diffuse, random, and point source. Sun et al. [9] propose a novel non-contact metamaterial beam solution for suppressing extremely low-frequency vibration and noise in precision instruments and equipment. The resonators of the metamaterial beams integrate a negative stiffness mechanism and an electromagnetic damping tuning system. Findings demonstrate that the negative stiffness can be effectively controlled by the nonlinear magnetic force between the magnets. Utilizing this mechanism, the bandgap frequency is successfully reduced to a minimum of 50 Hz. Furthermore, a method is proposed to combine electromagnetic damping and a negative impedance circuit to form a tuning system that can further lower the initial bandgap frequency to 4 Hz. Khorshidi et al. [10] investigated energy harvesting using vibrating honeycomb sandwich panels with auxetic core and carbon nanotube-reinforced face sheets. In this study, an energy harvester constructed from a honeycomb sandwich panel is examined. The modeled sandwich panel comprises an auxetic core and two carbon nanotube-reinforced face sheets. The findings demonstrate that this harvester offers greater flexibility in its stiffness, leading to enhanced energy harvesting performance. Ying et al. [11] successfully dampened vibrations by placing a magneto-rheological viscoelastic core inside a microbeam. They conducted various experiments on magneto-rheological viscoelastic materials, estimating their mechanical properties based on the intensity of the applied magnetic field. Utilizing the Galerkin method to solve the governing equations of microbeam vibrations, they extracted its dynamic response. In another study, vibrations of sandwich beams filled with magneto-rheological fluid under an external magnetic field were controlled by Joshi. [12] The researcher compared the natural frequencies and damping coefficients (free vibration analysis) as

well as the dynamic response (forced vibration analysis) of a sandwich beam with a magneto-rheological core to the corresponding values for an aluminum beam with similar dimensions. It was demonstrated that in all vibrational modes, the natural frequencies of the sandwich beam with the magneto-rheological core were higher than those of the aluminum beam. Aguib Et al. [13] investigated the dynamic behavior of sandwich panels with aluminum skins and a magneto-rheological core. They conducted various experiments to measure the rheological properties of the magneto-rheological material in the absence and presence of a magnetic field and examined the effects of the presence of ferromagnetic microparticles as well as the intensity of the applied magnetic field on the dynamic characteristics of the panels. Nayak et al. [14] investigated the dynamic stability of rotating sandwich beams with a magneto-rheological core using the finite element method. They assumed that the beam was subjected to a harmonic axial load and studied the effects of the applied magnetic field intensity on the beam's angular velocity and the radial axis to which the beam is connected on the spread of stable and unstable regions. Malekzadeh Fard et al. [15] investigated the free vibration analysis and dynamic response to the low-velocity impact of sandwich panels with a magneto-rheological core. They examined the effects of the applied magnetic field intensity on the natural frequencies and corresponding damping ratios in various vibration modes, as well as the deformation of the panel during impact and the force generated at the contact location. Ramamoorthy et al. [16] investigated the vibrations of sandwich panels with multi-layer composite skins and a rubber core, which was partially replaced with magneto-rheological fluid in some sections. They studied the effect of the applied magnetic field intensity on the natural frequencies of the panel in different vibration modes and the corresponding damping ratios for various boundary conditions. Furthermore, they extracted the dynamic response of such panels under external harmonic excitation. Eshaghi examined the influence of using a magneto-rheological core on the stability of the vibrations of panels subjected to external fluid flow (flutter analysis) [17, 18]. By employing a magneto-rheological fluid in the core of rectangular panels, he delayed the onset of the destructive flutter phenomenon in them. Alongside analytical results, he validated his modeling by conducting various experiments and observed that increasing the intensity of the applied magnetic field to the magneto-rheological core could delay the occurrence of the flutter phenomenon in the panel. In another study, he once again

investigated the effect of using a magneto-rheological fluid in the core of rectangular panels on the occurrence of the flutter phenomenon. However, in this research, only a portion of the core was filled with magneto-rheological fluid, as opposed to the entire core [19]. To delay the flutter phenomenon as much as possible (increasing the critical speed), he succeeded in determining the best position for the cube containing the magneto-rheological fluid inside the panel. He suggested that, to extend the critical speed as much as possible, the longest edge of the cube containing the magneto-rheological fluid should be aligned parallel to the fluid flow direction. Subramani et al. [20] investigated the free and forced vibrations of spherical sandwich shells with a magneto-rheological core and polymer coatings reinforced with CNTs. They demonstrated that to alter the natural frequency values of the shell, it is better to modify the mass fraction of the CNTs and to change the damping ratio of the shell, it is preferable to adjust the intensity of the magnetic field applied to the magneto-rheological core. In two similar studies, Houshang et al. [21] focused on analyzing the free vibrations and predicting the occurrence of the flutter phenomenon in incomplete conical shells with a magneto-rheological core. They observed that by increasing the intensity of the magnetic field applied to the magneto-rheological core, the natural frequencies and damping coefficients of the shell could be increased up to a certain level. However, with a further increase in the magnetic field intensity, due to core saturation, there would be little change in the natural frequencies and damping coefficients. Ghorbanpour Arani et al. [22] focused on analyzing flutter in sandwich panels with a magneto-rheological core and nano-composite coatings reinforced with GNPs. They observed that with an increase in the intensity of the magnetic field applied to the magneto-rheological core, there was a marginal increase in the critical velocity, and upon reaching core saturation, further improvement in the stability of the panel vibrations could not be observed. In a similar study, they investigated the stability of vibrations in moving sandwich panels with a magneto-rheological core and nano-composite coatings reinforced with GNPs [23]. One of the major weaknesses in magneto-rheological fluids and elastomers is their low stiffness (small shear modulus), leading to very large shear deformations in structures. To address this weakness, recently, an Indian researcher named R. Selvaraj, along with his colleagues attempted to add CNTs to MRE [24]. R. Selvaraj and M. Ramamoorthy conducted free vibration analysis of sandwich beams with magneto-rheological cores reinforced with CNTs using the finite

element method and various experimental tests. They observed that adding CNTs to the magneto-rheological core could increase the beam's natural frequencies. In another study, Selvaraj et al. [25] investigated the free vibrations of sandwich beams with a homogeneous core replaced in some sections with MREs reinforced with CNTs. They utilized a genetic algorithm to determine the optimal position for the MRE cube to maximize the beam's natural frequencies and the corresponding damping coefficients as much as possible. The dynamic behavior of cylindrical sandwich shells with a core of magneto-rheological material reinforced with CNTs and multilayer composite coatings was investigated by Arumugam et al. [26]. They observed that considering a specific thickness for the shell, increasing the thickness of the magneto-rheological core led to a reduction in the natural frequencies. However, a review of the research in this area indicates that the analysis of sandwich beams with a core of magneto-rheological material reinforced with CNTs and nano-composite coatings enhanced with GNPs has not yet been studied.

This study introduces a novel sandwich structure with an MRE core reinforced by carbon nanotubes (CNTs) and graphene nanoplatelet (GNP) face sheets, enhancing shear modulus and vibration control. It uniquely employs the Timoshenko beam model for improved accuracy in representing shear and angular deformations. Additionally, five GNP distribution patterns are examined to assess the effects on flexural stiffness and damping. The study further analyzes the combined impact of magnetic field intensity, viscoelastic foundation damping, and GNP face sheet thickness on natural frequencies and damping ratios, offering detailed insights for industrial applications. This combination of materials increases the shear modulus and enhances the structure's vibration control capability, making it suitable for high-pressure or high-vibration environments.

2. Geometry of the Problem and Mechanical Properties

As depicted in Fig.1, this study investigates the free vibrations of a three-layer sandwich beam supported on simple supports and resting on a viscoelastic foundation. The beam has a length of L and thickness h , consisting of a magnetorheological core reinforced with CNTs with a thickness of h_c , and two polymer layers reinforced with GNPs with thicknesses h_b and h_t . In deriving the governing equations for the vibrations of this structure, the following simplifying assumptions are considered:

- i). The amplitude of the beam's vibrations is much smaller compared to its dimensions, allowing us to analyze the vibrations in the linear range.
- ii). There is no slippage or separation between the layers of the beam.
- iii). The behavior of the foundation is linear.
- iv). The axial stiffness of the magnetorheological core is significantly smaller compared to the axial stiffness of the layers; thus, the magnetorheological core only has shear stiffness.
- v). In modeling the mechanical behavior of the magnetorheological core in free vibration analysis, a mixed shear modulus approach is used.

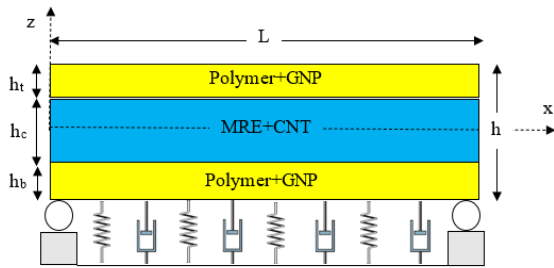


Fig. 1. Geometry of the problem under investigation

2.1. Mechanical Properties of the Core

Magneto-rheological MR materials are a class of smart materials whose mechanical properties can be altered by applying an external magnetic field. These materials exist in various states, including fluid, gel, foam, elastomer, and plastomer, with the most common being magneto-rheological fluids (MRFs) and MREs. MR fluids alter viscosity and yield stress under a magnetic field. This change in stiffness is primarily due to the interaction between the magnetic particles embedded in the elastomer matrix and the applied magnetic field. In shear flow conditions, they shift from liquid to semi-solid. While the application of a magnetic field

does affect the overall stiffness of the MRE, it's important to note that the most significant change occurs in the shear modulus, which represents the material's resistance to deformation under shear stress. Shear stiffness measures how they resist deformation. Primarily influencing shear properties. It is important to note that upon removal of the applied magnetic field, the changes in the mechanical properties of MR materials are rapidly reversed, and the material returns to its original state. According to the fourth assumption presented in Section 2.1, the only stress component (σ) in the magnetorheological core is the shear stress, which is expressed in terms of the corresponding shear strain component (γ) as follows [28]:

$$\sigma_{xz}^c = G_{xz}^c \gamma_{xz}^c, \tag{1}$$

In Eq. 1, G_{xz}^c presents the mixed shear modulus, which is expressed as follows [29]:

$$G_{xz}^c = G_0 (1 + j \eta_0) \tag{2}$$

In Eq. 2, G_0 and η_0 represent the storage shear modulus and the loss factor, respectively. It's worth mentioning that the subscript "c" refers to the core. For an MRE reinforced with multi-walled carbon nanotubes (MWCNTs), the values of storage shear modulus and loss factor for various fractions of MWCNTs and applied magnetic field intensity (B) are presented in Table 1. This table demonstrates that the storage shear modulus increases with an increasing fraction of MWCNTs and applied magnetic field intensity. Table 1. also shows that the loss factor increases with increasing magnetic field intensity, except for one exception, and generally increases with increasing fraction of MWCNTs. Therefore, it can be observed that adding CNTs to the MRE not only increases the structural stiffness but also improves its ability to dampen vibrations. In MATLAB software, using the curve fitting tool, the following equations can be proposed to estimate the data provided in Table 1:

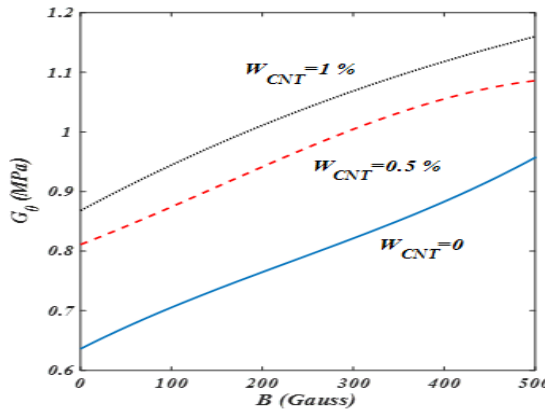
Table 1. Storage Shear Modulus and Loss Factor for an MWCNT Reinforced MRE [27]

B (Gauss)	W _{CNT} =0		W _{CNT} =0.005 (0.5 %)		W _{CNT} =0.01 (1 %)	
	G ₀ (MPa)	η ₀	G ₀ (MPa)	η ₀	G ₀ (MPa)	η ₀
0	0.636	0.0912	0.811	0.0926	0.868	0.0991
125	0.721	0.1038	0.891	0.1021	0.962	0.1120
250	0.793	0.1069	0.974	0.1100	1.041	0.1190
500	0.957	0.1099	1.086	0.1199	1.160	0.1261

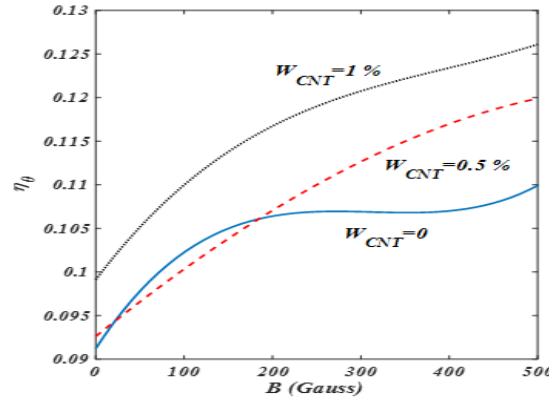
$$\begin{aligned}
 &W_{CNT} = 0: \\
 &G_0 (Pa) = 0.001259B^3 - 0.888B^2 + 771.3B + 636000, \\
 &\eta_0 = (5.397 \times 10^{-10})B^3 - (5.064 \times 10^{-7})B^2 + \\
 &\quad (1.557 \times 10^{-4})B + 0.0912, \\
 &W_{CNT} = 0.005 \text{ (0.5\%):} \\
 &G_0 (Pa) = -0.001344B^3 + 0.6B^2 + 586B + 811000, \\
 &\eta_0 = (-2.347 \times 10^{-11})B^3 - (4.24 \times 10^{-8})B^2 + \\
 &\quad (8.167 \times 10^{-5})B + 0.0926, \\
 &W_{CNT} = 0.01 \text{ (1\%):} \\
 &G_0 (Pa) = 0.000128B^3 - 0.528B^2 + 816B + 868000 \\
 &\eta_0 = (2.304 \times 10^{-10})B^3 - (2.752 \times 10^{-7})B^2 + \\
 &\quad (1.34 \times 10^{-4})B + 0.0991.
 \end{aligned} \tag{3}$$

It's important to note that similar equations are proposed in reference [27], which unfortunately do not match well with the data provided by them in Table 1. Several factors could contribute to variations in experimental and numerical results between different studies such as differences in material properties that even slight variations in the composition and the sandwich structures can lead to significant differences in mechanical behavior. Also testing conditions and procedures, modeling assumptions and simplifications, or Differences in the chosen model (e.g., Timoshenko vs. Euler-Bernoulli beam theory) can lead to variations in predicted behavior in some cases.

Figures 2(a) and 2(b) illustrate the changes in the shear storage modulus and damping ratio for the MRE reinforced with MWCNTs as a function of applied magnetic field intensity for different CNT mass fractions, respectively. Fig. 2(a) indicates that increasing applied magnetic field intensity increases the shear storage modulus for all CNT mass fractions. Additionally, Fig. 2(b) demonstrates that with increasing magnetic field intensity, the damping ratio increases when MWCNTs are added, but in the absence of MWCNTs in the MRE, an increasing behavior of the damping ratio along with oscillation is observed.



(a) Shear Storage Modulus



(b) Damping Ratio

Fig. 2. The effect of magnetic field intensity on the shear storage modulus and damping ratio of MWCNT-reinforced MRE

2.2. Mechanical Properties of Surface Layers

The present study employs graphene nanoplatelet GNP-reinforced polymer faces. To calculate the density (ρ) and Poisson's ratio (ν) of GNP-reinforced polymer faces, the mixing rule can be utilized as follows [30]:

$$\rho^i = \rho_{GNP}V_{GNP}^i + \rho_m V_m^i, \quad \nu^i = \nu_{GNP}V_{GNP}^i + \nu_m V_m^i, \quad i = b, t. \tag{4}$$

In Eq. 4, the subscripts GNP and m refer to GNPs and the polymer matrix, respectively, and V presents the volume fraction of the components. It's worth noting that the subscripts b and t Note the bottom and top layers of the beam, respectively. The volume fraction of (GNPs) can be calculated as follows based on their mass fraction (g_{GNP}) [31]:

$$V_{GNP}^i = \frac{g_{GNP}^i}{g_{GNP}^i + \frac{\rho_{GNP}}{\rho_m}(1 - g_{GNP}^i)}, \quad i = b, t. \tag{5}$$

The volume fraction of the polymer matrix can be calculated from the following equation [31,32]:

$$V_m^i = 1 - V_{GNP}^i, \quad i = b, t. \tag{6}$$

In this study, five different patterns for the distribution of GNPs in each of the matrices are considered.

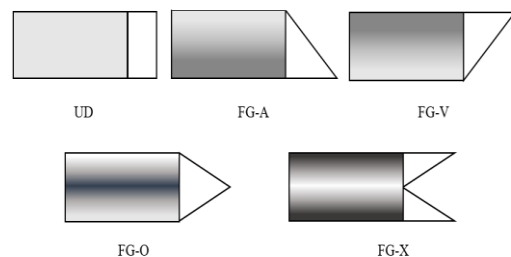


Fig. 3. Distribution patterns of GNPs in the matrices

These distribution patterns are illustrated in Fig. 3, where the higher the density of an area, the higher the number of GNPs added to that region. As observed, five patterns are considered as follows:

- A). Uniform Distribution (UD) Pattern: In this pattern, the mass fraction of GNPs is uniform across all regions.
- B). Graded Distribution FG-A Pattern: In this pattern, the mass fraction of GNPs at the top layer is zero and linearly increases to its maximum value at the bottom layer.
- C). Graded Distribution FG-V Pattern: In this pattern, the mass fraction of GNPs at the bottom layer is zero and linearly increases to its maximum value at the top layer.
- D). Graded Distribution FG-O Pattern: In this pattern, the mass fraction of GNPs at both the top and bottom layers is zero and linearly increases to its maximum value at the middle layer.
- E). Graded Distribution FG-X Pattern: In this pattern, the mass fraction of GNPs at the middle layer is zero and linearly increases to its maximum value at both the top and bottom layers.

Given the linear variation of the mass fraction of GNPs in these patterns, the following equations can be used to express the mass fraction of GNPs in these five distribution patterns [33]:

$$\begin{aligned}
 UD : \quad & g_{GNP}^i(z_i) = g_{GNP}^* \\
 FG - A : \quad & g_{GNP}^i(z_i) = \left(1 - \frac{2z_i}{h_i}\right) g_{GNP}^* \\
 FG - V : \quad & g_{GNP}^i(z_i) = \left(1 + \frac{2z_i}{h_i}\right) g_{GNP}^* \quad i = b, t. \quad (7) \\
 FG - O : \quad & g_{GNP}^i(z_i) = 2 \left(1 - \frac{2|z_i|}{h_i}\right) g_{GNP}^* \\
 FG - X : \quad & g_{GNP}^i(z_i) = 4 \frac{|z_i|}{h_i} g_{GNP}^*
 \end{aligned}$$

In Eq. 7, g_{GNP} represents the total mass fraction of GNPs. Using the following equation, it can be shown that Eq. 7 is adjusted in a way that the total mass fraction of GNPs is the same in all distribution patterns to ensure a fair comparison among them[33]:

$$g_{GNP}^* = \frac{1}{h_i} \int_{-\frac{h_i}{2}}^{\frac{h_i}{2}} g_{GNP}^i(z_i) dz_i, \quad i = b, t. \quad (8)$$

It is worth noting that Eq. 7 indicates that the total mass fraction of GNPs in the lower and upper layers of the beam is considered equal to each other.

The modulus of elasticity (E) of the beam's surfaces can be calculated using the Halpin-Tsai model as follows[33]:

$$E^i = \left(\frac{3}{8} \frac{1 + \xi_L \eta_L V_{GNP}^i}{1 - \eta_L V_{GNP}^i} + \frac{5}{8} \frac{1 + \xi_w \eta_w V_{GNP}^i}{1 - \eta_w V_{GNP}^i} \right) E_m, \quad i = b, t. \quad (9)$$

In Eq. 9 :

$$\eta_L = \frac{\eta - 1}{\eta + \xi_L}, \quad \eta_w = \frac{\eta - 1}{\eta + \xi_w}, \quad \xi_L = \frac{2l_{GNP}}{h_{GNP}}, \quad \xi_w = \frac{2w_{GNP}}{h_{GNP}}, \quad \eta = \frac{E_{GNP}}{E_m} \quad (10)$$

In Eq. 10, l_{GNP} , w_{GNP} , and h_{GNP} represent the length, width, and thickness of the GNPs, respectively.

3. Displacement Field

According to the first-order shear deformation theory (Timoshenko beam theory), the displacement field in the three layers of the beam can be considered as follows [34]:

$$\begin{aligned}
 u^i(x, z, t) &= u_0^i(x, t) + z_i \phi_0^i(x, t), \\
 w^i(x, z, t) &= w_0(x, t), \quad i = c, b, t. \quad (11)
 \end{aligned}$$

In Eq. 11, u and w represent the deformations in the x and z Directions, respectively. u_0 and w_0 denote the corresponding displacements on the midplane of each layer ($z_i=0$), and ϕ_0 represents the rotation.

With the condition of no sliding between the layers, the following equations can be expressed as continuity equations:

$$u^c\left(x, -\frac{h_c}{2}, t\right) = u^b\left(x, \frac{h_b}{2}, t\right), \quad u^c\left(x, \frac{h_c}{2}, t\right) = u^t\left(x, -\frac{h_t}{2}, t\right), \quad (12)$$

By substituting Eq. 11 into Eq. 12, the following equations can be obtained:

$$\begin{aligned}
 u_0^c(x, t) - \frac{h_c}{2} \phi_0^c(x, t) &= u_0^b(x, t) + \frac{h_b}{2} \phi_0^b(x, t), \\
 u_0^c(x, t) + \frac{h_c}{2} \phi_0^c(x, t) &= u_0^t(x, t) - \frac{h_t}{2} \phi_0^t(x, t), \quad (13)
 \end{aligned}$$

which, upon solving, leads to the following equations for longitudinal displacement and rotation in the core of the beam:

$$\begin{aligned}
 u_0^c(x, t) &= \frac{1}{2} [u_0^b(x, t) + u_0^t(x, t)] \\
 &\quad + \frac{h_b}{4} \phi_0^b(x, t) - \frac{h_t}{4} \phi_0^t(x, t), \\
 \phi_0^c(x, t) &= \frac{1}{h_c} [u_0^t(x, t) - u_0^b(x, t)] \\
 &\quad - \frac{h_b}{2h_c} \phi_0^b(x, t) - \frac{h_t}{2h_c} \phi_0^t(x, t), \quad (14)
 \end{aligned}$$

Substituting Eq. 14 into Eq. 11, the displacement field in the core can be written as:

$$u^c(x, z, t) = f_1(z_c)u_0^b(x, t) + \frac{h_b}{2}f_1(z_c)\phi_0^b(x, t) + f_2(z_c)u_0^t(x, t) - \frac{h_t}{2}f_2(z_c)\phi_0^t(x, t), \quad (15)$$

$$w^c(x, z, t) = w_0(x, t),$$

In Eq. 15, dimensionless functions f_1 and f_2 are defined as follows:

$$f_1(z_c) = \frac{1}{2} - \frac{z_c}{h_c}, \quad f_2(z_c) = \frac{1}{2} + \frac{z_c}{h_c}, \quad (16)$$

The values of these two functions at three specific levels within the core of the beam are provided in Table 2.

Table 2. Values of dimensionless functions f_1 and f_2 at the lower, upper, and middle levels of the core

	z_c/h_c	f_1	f_2
Bottom	-0.5	1	0
Middle	0	0	0.5
Top	0.5	0.5	1

4. Strain Components in the Core and Faces

As mentioned, in the core of the beam, the only existing component of strain is the shear strain component. This component of strain can be calculated as follows:

$$\gamma_{xz}^c = \frac{\partial u^c}{\partial z_c} + \frac{\partial w^c}{\partial x}. \quad (17)$$

By substituting Eq. 15 into Eq. 17, we can obtain the following equation:

$$\gamma_{xz}^c = f_1 u_0^b + \frac{h_b}{2} f_1 \phi_0^b + f_2 u_0^t - \frac{h_t}{2} f_2 \phi_0^t + \frac{\partial w_0}{\partial x}, \quad (18)$$

which, considering Eq. 17, is expressed as follows:

$$\gamma_{xz}^c = \frac{\partial w_0}{\partial x} - \frac{u_0^b}{h_c} - \frac{h_b}{2h_c} \phi_0^b + \frac{u_0^t}{h_c} - \frac{h_t}{2h_c} \phi_0^t, \quad (19)$$

The strain components in the layers of the beam can also be expressed as follows:

$$\epsilon_{xx}^i = \frac{\partial u^i}{\partial x},$$

$$\gamma_{xz}^i = \frac{\partial u^i}{\partial z_i} + \frac{\partial w^i}{\partial x}, \quad i = b, t. \quad (20)$$

Substituting Eq. 11 into it, we can obtain the following equation:

$$\epsilon_{xx}^i = \frac{\partial u_0^i}{\partial x} + z_i \frac{\partial \phi_0^i}{\partial x}, \quad i = b, t. \quad (21)$$

$$\gamma_{xz}^i = \phi_0^i + \frac{\partial w_0}{\partial x},$$

5. Stress Components in Core and Facing

The only stress component in the core of the beam is the shear stress component, which is given by Eq. 1. Substituting Eq. 19 into Eq. 1, this stress component in the beam core can be written as:

$$\sigma_{xz}^c = G_{xz}^c \left(\frac{\partial w_0}{\partial x} - \frac{u_0^b}{h_c} - \frac{h_b}{2h_c} \phi_0^b + \frac{u_0^t}{h_c} - \frac{h_t}{2h_c} \phi_0^t \right). \quad (22)$$

Stress Components on the Surfaces of the Beam can also be expressed as follows [34]:

$$\begin{Bmatrix} \sigma_{xx}^i \\ \sigma_{xz}^i \end{Bmatrix} = \begin{bmatrix} Q_{11}^i & 0 \\ 0 & k_s Q_{55}^i \end{bmatrix} \begin{Bmatrix} \epsilon_{xx}^i \\ \gamma_{xz}^i \end{Bmatrix}, \quad i = b, t. \quad (23)$$

In this relation,

$$Q_{11}^i = E^i, \quad Q_{55}^i = G^i = \frac{E^i}{2(1+\nu^i)}, \quad i = b, t. \quad (24)$$

It should be noted that G represents the shear modulus of the surfaces.

6. Hamilton's Principle

According to Hamilton's principle, if t_1 and t_2 are any two arbitrary times, and δ is considered as the variational operator, the governing equations and boundary conditions can be obtained from the following relation [35]:

$$\int_{t_1}^{t_2} (\delta T - \delta U_b + \delta W_{n.c.}) dt = 0, \quad (25)$$

In this equation, $Wn.c$, T , and U_b are the work of external non-conservative forces, kinetic energy, and strain energy, respectively.

The kinetic energy of the beam is calculated as follows:

$$T = \frac{1}{2} \iiint_{V_c} \rho^c \left[\left(\frac{\partial u^c}{\partial t} \right)^2 + \left(\frac{\partial w^c}{\partial t} \right)^2 \right] dV_c$$

$$+ \frac{1}{2} \iiint_{V_b} \rho^b \left[\left(\frac{\partial u^b}{\partial t} \right)^2 + \left(\frac{\partial w^b}{\partial t} \right)^2 \right] dV_b$$

$$+ \frac{1}{2} \iiint_{V_t} \rho^t \left[\left(\frac{\partial u^t}{\partial t} \right)^2 + \left(\frac{\partial w^t}{\partial t} \right)^2 \right] dV_t, \quad (26)$$

In Eq. 26, V represent the volume of each layer of the beam. Based on the following equation:

$$\begin{aligned} \iiint_{V_i} F(x, z_i) dV_i &= \int_{-\frac{h_c}{2}}^{\frac{h_c}{2}} \int_{-\frac{b}{2}}^{\frac{b}{2}} \int_0^L F(x, z_i) dx dy dz_i \\ &= b \int_0^L \int_{-\frac{h_c}{2}}^{\frac{h_c}{2}} F(x, z_i) dz_i dx, \quad i = c, b, t \end{aligned} \tag{27}$$

where (b) represents the width of the beam, Therefore, the kinetic energy relationship can be written as follows:

$$\begin{aligned} T &= \frac{b}{2} \int_0^L \left[I_{11}^c \left(\frac{\partial u_0^b}{\partial t} \right)^2 + 0.25 h_b^2 I_{11}^c \left(\frac{\partial \phi_0^b}{\partial t} \right)^2 + I_{22}^c \left(\frac{\partial u_0^t}{\partial t} \right)^2 + 0.25 h_t^2 I_{22}^c \left(\frac{\partial \phi_0^t}{\partial t} \right)^2 \right. \\ &\quad + h_b I_{11}^c \frac{\partial u_0^b}{\partial t} \frac{\partial \phi_0^b}{\partial t} + 2 I_{12}^c \frac{\partial u_0^b}{\partial t} \frac{\partial u_0^t}{\partial t} - h_t I_{12}^c \frac{\partial u_0^b}{\partial t} \frac{\partial \phi_0^t}{\partial t} + h_b I_{12}^c \frac{\partial \phi_0^b}{\partial t} \frac{\partial u_0^t}{\partial t} \\ &\quad - 0.5 h_b h_t I_{12}^c \frac{\partial \phi_0^b}{\partial t} \frac{\partial \phi_0^t}{\partial t} - h_t I_{22}^c \frac{\partial u_0^t}{\partial t} \frac{\partial \phi_0^t}{\partial t} + I_{00}^c \left(\frac{\partial w_0}{\partial t} \right)^2 + I_0^b \left(\frac{\partial u_0^b}{\partial t} \right)^2 \\ &\quad + 2 I_1^b \frac{\partial u_0^b}{\partial t} \frac{\partial \phi_0^b}{\partial t} + I_2^b \left(\frac{\partial \phi_0^b}{\partial t} \right)^2 + I_0^t \left(\frac{\partial w_0}{\partial t} \right)^2 + I_0^t \left(\frac{\partial u_0^t}{\partial t} \right)^2 \\ &\quad \left. + 2 I_1^t \frac{\partial u_0^t}{\partial t} \frac{\partial \phi_0^t}{\partial t} + I_2^t \left(\frac{\partial \phi_0^t}{\partial t} \right)^2 + I_0^t \left(\frac{\partial w_0}{\partial t} \right)^2 \right] dx, \end{aligned} \tag{28}$$

In equ. 28

$$\begin{aligned} I_{ij}^c &= \rho^c \int_{-\frac{h_c}{2}}^{\frac{h_c}{2}} f_i f_j dz_c, \quad I_i^b = \int_{-\frac{h_b}{2}}^{\frac{h_b}{2}} \rho^b(z_b) z_b^i dz_b \\ I_i^t &= \int_{-\frac{h_t}{2}}^{\frac{h_t}{2}} \rho^t(z_t) z_t^i dz_t, \quad i, j = 0, 1, 2 \end{aligned} \tag{29}$$

The strain energy of the beam can be expressed as follows:

$$\begin{aligned} U_b &= \frac{1}{2} \iiint_{V_c} \sigma_{xz}^c \gamma_{xz}^c dV_c + \frac{1}{2} \iiint_{V_b} (\sigma_{xx}^b \varepsilon_{xx}^b + \sigma_{xz}^b \gamma_{xz}^b) dV_b \\ &\quad + \frac{1}{2} \iiint_{V_t} (\sigma_{xx}^t \varepsilon_{xx}^t + \sigma_{xz}^t \gamma_{xz}^t) dV_t, \end{aligned} \tag{30}$$

In Eq. 30, the stress resultants are defined as follows:

$$Q_{xz}^c = \int_{-\frac{h_c}{2}}^{\frac{h_c}{2}} \sigma_{xz}^c dz_c, \tag{31}$$

$$\begin{aligned} \begin{Bmatrix} N_{xx}^i \\ M_{xx}^i \end{Bmatrix} &= \int_{-\frac{h_i}{2}}^{\frac{h_i}{2}} \sigma_{xx}^i \begin{Bmatrix} 1 \\ z_i \end{Bmatrix} dz_i, \\ &\quad i = b, t. \end{aligned} \tag{32}$$

$$Q_{xz}^i = \int_{-\frac{h_i}{2}}^{\frac{h_i}{2}} \sigma_{xz}^i dz_i$$

By substituting Eq. 22 into Eq. 32, the stress resultant in the core of the beam can be expressed as follows:

$$Q_{xz}^c = A^c \left(\frac{\partial w_0}{\partial x} - \frac{u_0^b}{h_c} - \frac{h_b}{2 h_c} \phi_0^b + \frac{u_0^t}{h_c} - \frac{h_t}{2 h_c} \phi_0^t \right), \tag{33}$$

in Eq. 33

$$A^c = G_{xz}^c h_c, \tag{34}$$

Similarly, stress resultants in beam sections are calculated as follows:

$$N_{xx}^i = A_{11}^i \frac{\partial u_0^i}{\partial x} + B_{11}^i \frac{\partial \phi_0^i}{\partial x}, \quad M_{xx}^i = B_{11}^i \frac{\partial u_0^i}{\partial x} + D_{11}^i \frac{\partial \phi_0^i}{\partial x}, \tag{35}$$

$$Q_{xz}^i = k_s A_{55}^i \left(\phi_0^i + \frac{\partial w_0}{\partial x} \right), \quad i = b, t.$$

in Eq. 35:

$$\begin{Bmatrix} A_{ij}^i \\ B_{ij}^i \\ D_{ij}^i \end{Bmatrix} = \int_{-\frac{h_i}{2}}^{\frac{h_i}{2}} Q_{ij}^i \begin{Bmatrix} 1 \\ z_i \\ z_i^2 \end{Bmatrix} dz_i, \quad i = b, t, \quad j = 1, 5. \tag{36}$$

Due to the presence of friction at the support, the force generated by it is a non-conservative force. The work done by this non-conservative force can be expressed as follows:

$$W_{n.c.} = b \int_0^L q_f w_0 dx, \tag{37}$$

In Eq. 37, q_f represents the reactive force of the support, which is expressed according to the viscoelastic model and Eq. 36 as follows [36]:

$$q_f = -k_w w_0 + k_p \frac{\partial^2 w_0}{\partial x^2} - c \frac{\partial w_0}{\partial t}, \tag{38}$$

In Eq. 38, k_w , k_p , and c are recognized as the coefficients of the Winkler bed, the Pasternak bed, and the damping coefficients of the bed, respectively.

Boundary conditions at both ends of the beam can generally be expressed as follows:

$$\begin{aligned} (Q_{xz}^c + Q_{xz}^b + Q_{xz}^t) \delta w_0 &= 0, \\ N_{xx}^b \delta u_0^b &= 0, \quad M_{xx}^b \delta \phi_0^b = 0, \quad N_{xx}^t \delta u_0^t = 0, \quad M_{xx}^t \delta \phi_0^t = 0. \end{aligned} \tag{39}$$

In this study, simple boundary conditions are investigated. In this case, the boundary condition equations are expressed as follows:

$$w_0 = 0, \quad N_{xx}^b = 0, \quad M_{xx}^b = 0, \quad N_{xx}^t = 0, \quad M_{xx}^t = 0, \tag{40}$$

Based on the preceding discussion, the equations of motion can be derived as follows:

$$\begin{aligned} \delta w_0^c : \\ (A^c + k_s A_{55}^b + k_s A_{55}^t + k_p) \frac{\partial^2 w_0}{\partial x^2} - k_w w_0 - c \frac{\partial w_0}{\partial t} - \frac{A^c}{h_c} \frac{\partial u_0^b}{\partial x} \\ - \left(\frac{h_b}{2 h_c} A^c - k_s A_{55}^b \right) \frac{\partial \phi_0^b}{\partial x} + \frac{A^c}{h_c} \frac{\partial u_0^t}{\partial x} - \left(\frac{h_t}{2 h_c} A^c - k_s A_{55}^t \right) \frac{\partial \phi_0^t}{\partial x} \\ - (I_{00}^c + I_0^b + I_0^t) \frac{\partial^2 w_0}{\partial t^2} = 0, \end{aligned} \tag{41}$$

$$\delta u_0^b : \frac{A^c}{h_c} \frac{\partial w_0}{\partial x} + A_{11}^b \frac{\partial^2 u_0^b}{\partial x^2} - \frac{A^c}{h_c^2} u_0^b + B_{11}^b \frac{\partial^2 \phi_0^b}{\partial x^2} - \frac{h_b}{2h_c^2} A^c \phi_0^b + \frac{A^c}{h_c^2} u_0^b - \frac{h_b}{2h_c^2} A^c \phi_0^b - (I_{11}^c + I_0^b) \frac{\partial^2 u_0^b}{\partial t^2} - (0.5h_b I_{11}^c + I_1^b) \frac{\partial^2 \phi_0^b}{\partial t^2} - I_{12}^c \frac{\partial^2 u_0^b}{\partial t^2} + 0.5h_b I_{12}^c \frac{\partial^2 \phi_0^b}{\partial t^2} = 0,$$

$$\delta \phi_0^b : \left(\frac{h_b}{2h_c} A^c - k_s A_{35}^b \right) \frac{\partial w_0}{\partial x} + B_{11}^b \frac{\partial^2 u_0^b}{\partial x^2} - \frac{h_b}{2h_c^2} A^c u_0^b + D_{11}^b \frac{\partial^2 \phi_0^b}{\partial x^2} - \left(\frac{h_b^2}{4h_c^2} A^c + k_s A_{35}^b \right) \phi_0^b + \frac{h_b}{2h_c^2} A^c u_0^b - \frac{h_b h_c}{4h_c^2} A^c \phi_0^b - (0.5h_b I_{11}^c + I_1^b) \frac{\partial^2 u_0^b}{\partial t^2} - (0.25h_b^2 I_{11}^c + I_2^b) \frac{\partial^2 \phi_0^b}{\partial t^2} - 0.5h_b I_{12}^c \frac{\partial^2 u_0^b}{\partial t^2} + 0.25h_b h_c I_{12}^c \frac{\partial^2 \phi_0^b}{\partial t^2} = 0,$$

$$\delta u_0^t : -\frac{A^c}{h_c} \frac{\partial w_0}{\partial x} + \frac{A^c}{h_c^2} u_0^b + \frac{h_b}{2h_c^2} A^c \phi_0^b + A_{11}^t \frac{\partial^2 u_0^t}{\partial x^2} - \frac{A^c}{h_c^2} u_0^t + B_{11}^t \frac{\partial^2 \phi_0^t}{\partial x^2} + \frac{h_b}{2h_c^2} A^c \phi_0^t - I_{12}^c \frac{\partial^2 u_0^b}{\partial t^2} - 0.5h_b I_{12}^c \frac{\partial^2 \phi_0^b}{\partial t^2} - (I_{22}^c + I_0^t) \frac{\partial^2 u_0^t}{\partial t^2} + (0.5h_b I_{22}^c - I_1^t) \frac{\partial^2 \phi_0^t}{\partial t^2} = 0,$$

$$\delta \phi_0^t : \left(\frac{h_b}{2h_c} A^c - k_s A_{35}^t \right) \frac{\partial w_0}{\partial x} - \frac{h_b}{2h_c^2} A^c u_0^b - \frac{h_b h_c}{4h_c^2} A^c \phi_0^b + B_{11}^t \frac{\partial^2 u_0^t}{\partial x^2} + \frac{h_b}{2h_c^2} A^c u_0^t + D_{11}^t \frac{\partial^2 \phi_0^t}{\partial x^2} - \left(\frac{h_b^2}{4h_c^2} A^c + k_s A_{35}^t \right) \phi_0^t + 0.5h_b I_{12}^c \frac{\partial^2 u_0^b}{\partial t^2} + 0.25h_b h_c I_{12}^c \frac{\partial^2 \phi_0^b}{\partial t^2} + (0.5h_b I_{22}^c - I_1^t) \frac{\partial^2 u_0^t}{\partial t^2} - (0.25h_b^2 I_{22}^c + I_2^t) \frac{\partial^2 \phi_0^t}{\partial t^2} = 0,$$

Using a similar approach, by substituting Eqs. 33 and 35 into the boundary conditions 40, these equations can be written as follows:

$$w_0 = 0, \quad A_{11}^b \frac{\partial u_0^b}{\partial x} + B_{11}^b \frac{\partial \phi_0^b}{\partial x} = 0, \quad B_{11}^b \frac{\partial u_0^b}{\partial x} + D_{11}^b \frac{\partial \phi_0^b}{\partial x} = 0, \quad (42)$$

$$A_{11}^t \frac{\partial u_0^t}{\partial x} + B_{11}^t \frac{\partial \phi_0^t}{\partial x} = 0, \quad B_{11}^t \frac{\partial u_0^t}{\partial x} + D_{11}^t \frac{\partial \phi_0^t}{\partial x} = 0.$$

The boundary conditions (Eq. 42) can also be expressed in simplified form as follows:

$$w_0 = 0, \quad \frac{\partial u_0^b}{\partial x} = 0, \quad \frac{\partial \phi_0^b}{\partial x} = 0, \quad \frac{\partial u_0^t}{\partial x} = 0, \quad \frac{\partial \phi_0^t}{\partial x} = 0, \quad (43)$$

7. Solving the Governing Equations

According to the Navier method, boundary conditions (Eq. 43) can be established at both ends of the beam using the following form of solutions:

$$\begin{Bmatrix} u_0^b(x,t) \\ u_0^t(x,t) \\ \phi_0^b(x,t) \\ \phi_0^t(x,t) \end{Bmatrix} = \begin{Bmatrix} U^b \\ U^t \\ \Phi^b \\ \Phi^t \end{Bmatrix} e^{j\omega_n t} \cos(\alpha x), \quad (44)$$

$$w_0(x,t) = W e^{j\omega_n t} \sin(\alpha x),$$

In Eq. 44, ω_n represents an eigenvalue, $j^2 = -1$, and

$$\alpha = \frac{n\pi}{L}, \quad n = 1, 2, 3, \dots \quad (45)$$

It should be noted that in Eq. 45, the variable $n = 1, 2, 3, \dots$ is known as the mode number, and the subscript n in ω_n indicates the eigenvalue of the beam in the n th vibration mode. By substituting Eq. 44 into the governing Eq. 41, we can obtain the following system of algebraic equations for the eigenvalues:

$$([K] + j\omega_n [C] + \omega_n^2 [M]) \{s\} = \{0\}, \quad n = 1, 2, 3, \dots \quad (46)$$

In Eq. 46, the mass ($[M]$), damping ($[C]$), and stiffness ($[K]$) matrices and the displacement vector are defined as follows:

$$\{s\} = \begin{Bmatrix} W \\ U^b \\ \Phi^b \\ U^t \\ \Phi^t \end{Bmatrix}, \quad [K] = \begin{bmatrix} k_{11} & k_{12} & k_{13} & k_{14} & k_{15} \\ & k_{22} & k_{23} & k_{24} & k_{25} \\ & & k_{33} & k_{34} & k_{35} \\ \text{sym} & & & k_{44} & k_{45} \\ & & & & k_{55} \end{bmatrix}, \quad [C] = \begin{bmatrix} -jc & 0 & 0 & 0 & 0 \\ & 0 & 0 & 0 & 0 \\ & & 0 & 0 & 0 \\ & & & \text{sym} & 0 & 0 \\ & & & & & 0 \end{bmatrix}, \quad (47)$$

$$[M] = \begin{bmatrix} I_{00}^c + I_0^b + I_0^t & 0 & 0 & 0 & 0 \\ & I_{11}^c + I_0^b & 0.5h_b I_{11}^c + I_1^b & I_{12}^c & -0.5h_b I_{12}^c \\ & & 0.25h_b^2 I_{11}^c + I_2^b & 0.5h_b I_{12}^c & -0.25h_b h_c I_{12}^c \\ \text{sym} & & & I_{22}^c + I_0^t & -0.5h_b I_{22}^c + I_1^t \\ & & & & 0.25h_b^2 I_{22}^c + I_2^t \end{bmatrix}$$

In Eq. 47

$$k_{11} = -\alpha^2 (A^c + k_s A_{35}^b + k_s A_{35}^t + k_p) - k_w, \quad k_{12} = \alpha \frac{A^c}{h_c},$$

$$k_{13} = \alpha \left(\frac{h_b}{2h_c} A^c - k_s A_{35}^b \right), \quad k_{14} = -\alpha \frac{A^c}{h_c},$$

$$k_{15} = \alpha \left(\frac{h_b}{2h_c} A^c - k_s A_{35}^t \right), \quad k_{22} = -\left(\alpha^2 A_{11}^b + \frac{A^c}{h_c^2} \right),$$

$$k_{23} = -\left(\alpha^2 B_{11}^b + \frac{h_b}{2h_c^2} A^c \right), \quad k_{24} = \frac{A^c}{h_c^2},$$

$$k_{25} = -\frac{h_b}{2h_c^2} A^c, \quad k_{33} = -\left(\alpha^2 D_{11}^b + \frac{h_b^2}{4h_c^2} A^c + k_s A_{35}^b \right),$$

$$k_{34} = \frac{h_b}{2h_c^2} A^c, \quad k_{35} = -\frac{h_b h_c}{4h_c^2} A^c,$$

$$k_{44} = -\left(\alpha^2 A_{11}^t + \frac{A^c}{h_c^2} \right), \quad k_{45} = -\left(\alpha^2 B_{11}^t - \frac{h_b}{2h_c^2} A^c \right),$$

$$k_{55} = -\left(\alpha^2 D_{11}^t + \frac{h_b^2}{4h_c^2} A^c + k_s A_{35}^t \right).$$

By solving the eigenvalue problem (Eq. 46) for each value of n , The eigenvalues of the beam can be obtained for different vibration modes. These eigenvalues are generally complex numerical values, and using them, the natural frequencies of the beam vibrations Ω_n in different modes and the corresponding damping coefficients η_n can be calculated as follows:

$$\Omega_n = \sqrt{\text{Re}(\omega_n^2)}, \quad \eta_n = \frac{\text{Im}(\omega_n^2)}{\text{Re}(\omega_n^2)}. \quad (49)$$

where Re and Im refer to the real and imaginary parts of a complex number, respectively.

8. Numerical Results

In the following section, numerical results are presented. Initially, the accuracy of the analysis presented in this study is evaluated by comparing it with the results reported by other researchers in specific cases. Then, the effect of beam and bed characteristics on the natural frequencies of beam vibrations and the corresponding damping coefficients is investigated. Except in cases explicitly mentioned, the following dimensionless definitions are used for the natural frequencies of beam vibrations and bed coefficients:

$$\lambda_n = \Omega_n L \sqrt{\frac{\rho_m}{E_m}}, \quad k_w^* = \frac{k_w L}{E_m}, \quad k_p^* = \frac{k_p}{E_m L}, \quad c^* = \frac{c}{\sqrt{\rho_m E_m}}. \quad (50)$$

Additionally, unless explicitly stated otherwise, the beam and bed characteristics are considered as follows [33]:

Beam	$L = 1m, \quad \frac{h_b}{L} = \frac{h_c}{L} = 0.02, \quad \frac{h_t}{L} = 0.05.$
Core	$W_{CNT} = 1\%, \quad B = 500Gauss, \quad \rho_c = 3500 \frac{kg}{m^3}.$
Face sheets	$E_m = 3GPa, \quad \nu_m = 0.34, \quad \rho_m = 1200 \frac{kg}{m^3}.$
GNP (XX)	$E_{GNP} = 1.01TPa, \quad \nu_{GNP} = 0.186, \quad \rho_{GNP} = 1060 \frac{kg}{m^3},$ $l_{GNP} = 2.5 \mu m, \quad w_{GNP} = 1.5 \mu m, \quad h_{GNP} = 1.5 nm,$ $g_{GNP}^* = 0.01.$
Foundation	$k_w^* = 0.1, \quad k_p^* = 0.01, \quad c^* = 0.1.$

8.1. Verification

Consider a sandwich beam with an MR core and homogeneous concentric circular surfaces.

The geometric specifications of the beam are given as $L=0.3m$ and $h_b = h_c = h_t = 5mm$, where h_b , h_c , and h_t represent the thickness of the bottom, core, and top layers, respectively. The surfaces of the beam are made of aluminum with the following mechanical properties: $E = 68GPa$, $\nu = 0.3077$, and $\rho = 2700 kg/m^3$. The density of the MR core is $\rho_c = 3500 kg/m^3$, and its shear modulus varies as a function of the applied magnetic field as follows [37]:

$$G_{xz}^c = G' + jG''$$

$$G' = -3.3691B^2 + 4997.5B + 893000 Pa, \quad (51)$$

$$G'' = -0.9B^2 + 812.4B + 185500 Pa.$$

For various values of applied magnetic field intensity, the values of beam vibration frequencies in Hertz are presented in Table 3. alongside the values reported by Rajamohan et al. [37]. As observed, there is a very high level of agreement between the results, indicating the accuracy of the analysis presented in this study. Some discrepancies can be found between the outcomes which could be Variations in the computational or analytical methods used to calculate the vibration frequencies or differences in the assumed material properties, such as density, elasticity, damping, boundary conditions, and constraints, which can lead to differences in results. Also, approximation methods, round-off errors, or simplifications used in the numerical analysis can contribute to small percentage differences. The percentage differences between the studies are relatively small, indicating that while there are discrepancies, the overall trends and behaviors are consistent between the analyses.

Table. 3 Vibration Frequencies of MR Sandwich Beam with Aluminum Surfaces in Hertz

B (Guass)		n=1	n=2	n=3	n=4	n=5
0	The presented analysis	103.92	398.92	888.52	1570.11	2440.01
	Rajamohan et al. [37]	104.28	396.96	882.36	1557.60	2419.30
	Percentage Difference (%)	-0.35	0.49	0.70	0.80	0.86
100	The presented analysis	106.62	401.8	891.43	1573.03	2442.92
	Rajamohan et al. [37]	106.72	399.54	884.98	1560.20	2421.90
	Percentage Difference (%)	-0.09	0.57	0.73	0.82	0.87
200	The presented analysis	108.86	404.24	893.91	1575.52	2445.41
	Rajamohan et al. [37]	108.76	401.73	887.21	1562.50	2424.10
	Percentage Difference (%)	0.09	0.62	0.76	0.83	0.88
300	The presented analysis	110.66	406.25	895.96	1577.58	2447.47
	Rajamohan et al. [37]	110.43	403.54	889.05	1564.30	2426.00
	Percentage Difference (%)	0.21	0.67	0.78	0.85	0.89

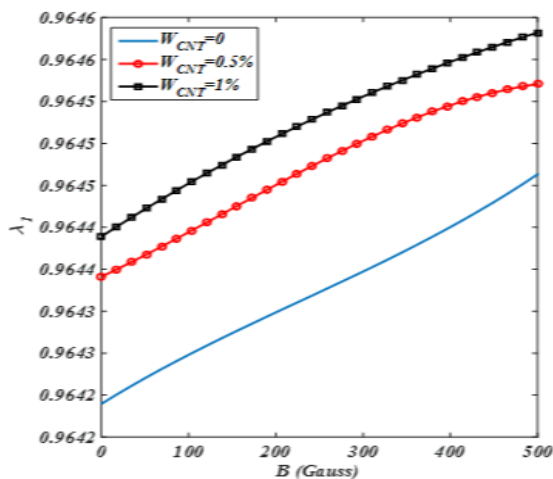
8.2. Impact of Magnetic Field Intensity

Figure 2 illustrates that the applied magnetic field intensity increases the shear storage modulus and the core loss factor.

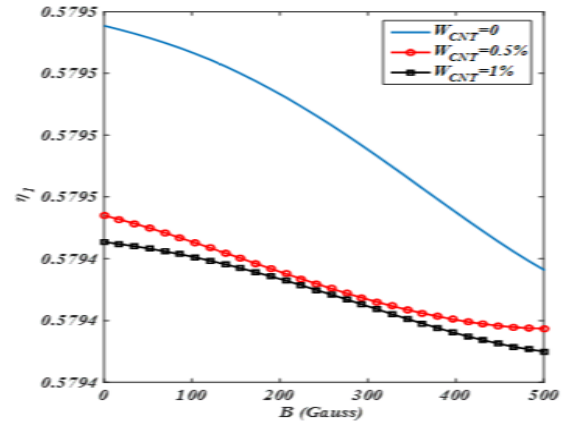
The effect of the magnetic field intensity on the natural vibration frequencies of the beam and the beam damping coefficients for different masses of CNTs added to the magnetorheological core is investigated in Fig. 4. As expected, with increasing applied magnetic field intensity to the core and increasing shear storage modulus, the stiffness of the beam increases, which leads to an increase in the natural magnetic-rheological vibration frequencies in the first vibration mode. On the other hand, the increase in the core loss factor leads to an increase in the beam damping coefficient, while on the other hand, the increase in the shear storage modulus (increase in stiffness) of the core leads to a decrease in the beam damping coefficient.

Therefore, as shown in Fig. 4, the beam damping coefficients in the first mode decrease due to the interaction of these two effects.

Figure 4 shows that an increase in the volume mass of CNTs added to the magnetorheological core is observed to increase the natural vibration frequencies of the beam. However, for the effect of the volume mass CNTs added to the magnetorheological core on the corresponding damping coefficients, the damping coefficient decreases with increasing volume mass CNTs added to the magnetorheological core, depending on the applied magnetic field intensity.



(a) Resonant Frequencies



(b) Damping Coefficients

Fig. 4. The effect of magnetic field intensity on the natural frequencies and damping coefficients of the beam for various mass fractions of CNTs added to the MR core

Figure 4(a) shows that for $W_{CNT} = 1\%$, with an increase in magnetic field intensity from zero to 500 Gauss, the frequency of MR beam vibrations in the first mode ($n=1$) increases by less than 0.03%, and the corresponding damping coefficient (Fig.4(a)) decreases by about 0.006%. On the other hand, Fig.4(a) indicates that for $B=500$ Gauss, with an increase in the mass fraction of CNTs from zero to 1%, the frequency of magneto-rheological beam vibrations in the first mode ($n=1$) increases by less than 0.02%, and the corresponding damping coefficient (Fig.4(b)) by less than 0.005%. In other words, the effect of magnetic field intensity applied to the magneto-rheological core on the natural frequencies of vibrations and damping coefficients of the beam is very small, attributed to the weak magneto-rheological effect of the MREs, as mentioned earlier. Additionally, it can be observed that the increase in and addition of CNTs to the magneto-rheological core does not result in significant growth in the natural frequencies of beam vibrations and damping coefficients. Considering the high cost of (CNTs), reinforcing the beam by adding CNTs to the magneto-rheological core may not be very cost-effective.

8.3. Effect of Thickness of GNPs Reinforced Face Sheets

Figure 5 (a) investigates the effect of GNP-reinforced facing thickness on the vibration frequencies and Fig. 5 (b) damping coefficients of the beam for different thicknesses of the MR core.

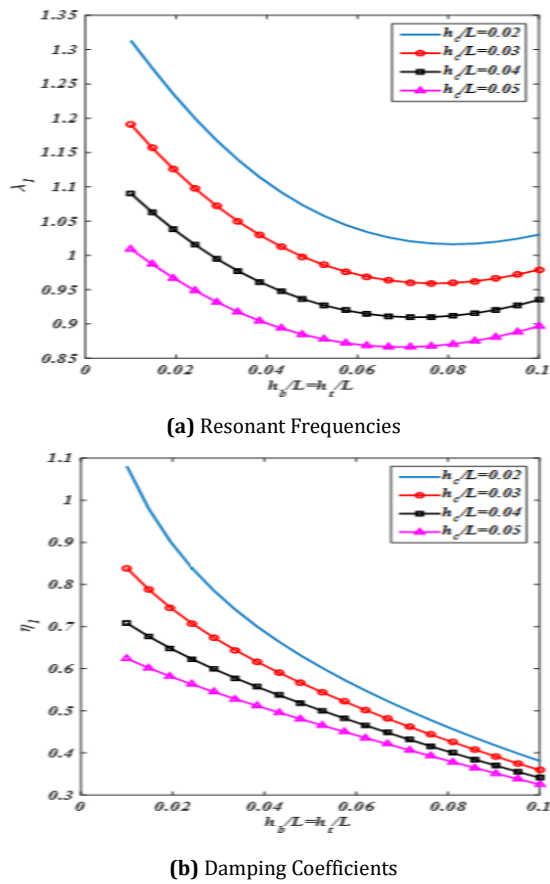


Fig. 5. The influence of GNPs -reinforced faces thickness on the natural frequencies and damping coefficients of the beam for various thicknesses of the MR core

Increasing the thickness of GNP-reinforced coatings leads to a significant increase in the beam stiffness as well as its mass. Therefore, the interplay between these two factors determines whether the flexural vibration frequencies of the beam increase or decrease with increasing thickness of GNP-reinforced coatings. Fig.5 (a) illustrates this interplay and states that with increasing thickness of GNP-reinforced coatings, the flexural vibration frequencies of the beam initially decrease, indicating the effect of increased mass over stiffness enhancement. However, as the thickness of GNP-reinforced

coatings further increases and both the stiffness and mass of the beam grow simultaneously, the flexural vibration frequencies of the beam increase. In other words, for the first vibration mode and depending on the MR core thickness, there exists a specific thickness of the coatings that results in the lowest flexural vibration frequencies in that vibration mode. Additionally, Fig. 5 (b) shows that with increasing thickness of GNP-reinforced coatings and simultaneous growth of stiffness and mass of the beam, the damping coefficients of the beam in the first vibration mode decrease.

Table 4. investigates the effect of graphene nanoplatelet distribution patterns in the nanocomposite coatings on the frequencies of flexural vibrations and corresponding damping coefficients of the beam. As indicated in Table 4, the highest values of resonant frequencies and the lowest values of damping coefficients belong to the XX distribution pattern, while the lowest resonant frequencies and the highest damping coefficients belong to the OO distribution pattern.

To explain this difference, it can be noted that the distribution pattern of GNPs does not affect the mass of the coatings, but as GNPs are distributed further away from the mid-surface of the coatings, the flexural stiffness of the coatings increases. Therefore, the highest values of resonant frequencies and the lowest values of damping coefficients belong to the XX distribution pattern, while the OO distribution pattern exhibits the opposite behavior. According to the data in Table 4., it can be concluded that by changing the distribution pattern of GNPs in the nanocomposite coatings from the OO to the XX state, the frequency of the beam's flexural vibrations in the first mode ($n=1$) increases by approximately 0.12%, while the corresponding damping coefficient decreases only by about 0.02%. In other words, the distribution pattern of GNPs in the nanocomposite coatings has little effect on the resonant frequencies of the beam's flexural vibrations and the corresponding damping coefficients.

Table 4. The effect of (GNPs) distribution patterns in coatings on resonant frequencies and corresponding damping coefficients

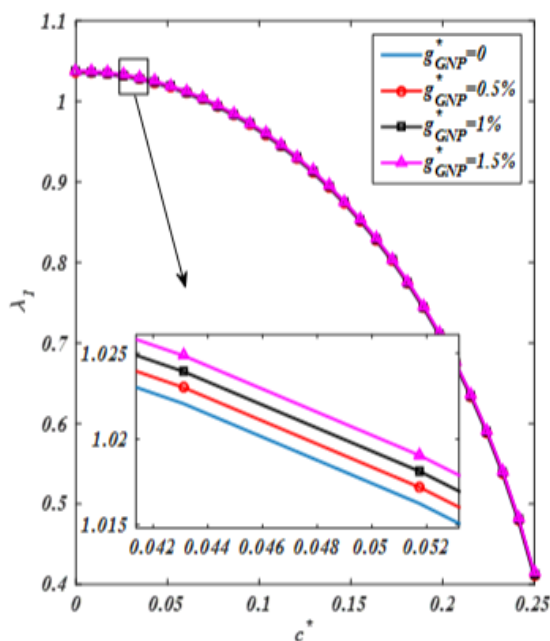
		UU	AA	XX	OO	AV	VA
λ_n	$n=1$	0.9640	0.9637	0.9646	0.9634	0.9638	0.9636
	$n=2$	1.6035	1.6004	1.6093	1.5978	1.6005	1.6005
	$n=3$	2.3281	2.3172	2.3478	2.3080	2.3168	2.3184
	$n=4$	3.1046	3.0791	3.1504	3.0576	3.0775	3.0824
η_n	$n=1$	0.5798	0.5800	0.5794	0.5802	0.5799	0.5801
	$n=2$	0.3403	0.3409	0.3391	0.3416	0.3408	0.3411
	$n=3$	0.2325	0.2334	0.2305	0.2345	0.2333	0.2336
	$n=4$	0.1735	0.1748	0.1710	0.1762	0.1747	0.1750

It seems that the reason for this is the small thickness of the face sheets compared to the core thickness of the beam. Although the change is small, the relationship between GNP distribution and vibration frequency is consistent with findings from previous studies and supports the effectiveness of this approach for specific applications.

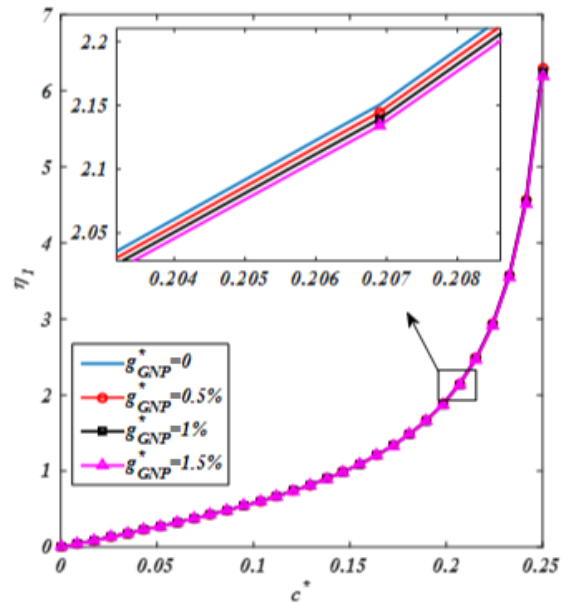
8.4. The Effect of Damping Ratio

Figure 6 (a) investigates the effect of GNP volume fraction on the resonant frequencies and Fig. 6 (b) corresponding damping coefficients of the beam for different substrate damping ratios. Due to the significantly high elasticity modulus of GNPs compared to the polymer matrix of the coatings, increasing the GNP volume fraction leads to a considerable increase in the beam stiffness. Consequently, this results in an increase in the resonant frequencies of the beam's vibrations in the first vibration mode and a decrease in the corresponding damping coefficients.

Additionally, Fig. 6 illustrates that with increasing substrate damping ratio, the resonant frequencies of the beam's vibrations in the first vibration mode decrease, while the corresponding damping coefficients increase. Figure 6 (a) illustrates that for $g_{GNP}^* = 1.5\%$, increasing the dimensionless damping coefficient of the substrate from zero to 0.25 decreases the first-mode ($n=1$) damped natural frequency of the beam vibrations by about 60%, while the corresponding damping ratio (Fig.6 (b)) experiences a significant increase (about 26.6 million percent).



(a) Resonant Frequencies



(b) Damping Coefficients

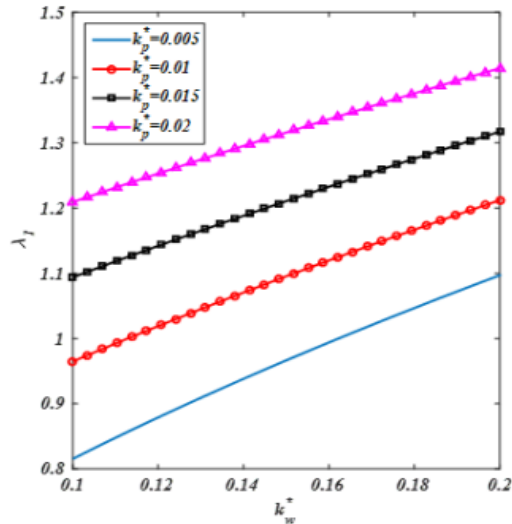
Fig. 6. The effect of viscoelastic foundation on the Natural Frequencies and Damping Coefficients of the Beam for various values of the mass fraction of GNPs.

In other words, the effect of the substrate damping coefficient on the damped natural frequencies of the beam vibrations is significant, and the corresponding damping ratios are very significant. Figure 6 (a) also shows that for $c^* = 0.25$, increasing the mass fraction of GNPs from zero to 1.5% increases the first-mode ($n=1$) damped natural frequency of the vibrations by about 1.5%, while the corresponding damping ratio (Fig. 6 (b)) decreases by about 2.5%. A comparison of the increase in the damped natural frequencies of the beam vibrations in Figs. 6 and 4 reveals that if the goal is to increase the natural frequencies of the beam as much as possible, adding GNPs to the polymer surfaces of the beam is much more effective than adding CNTs to its magnetorheological core.

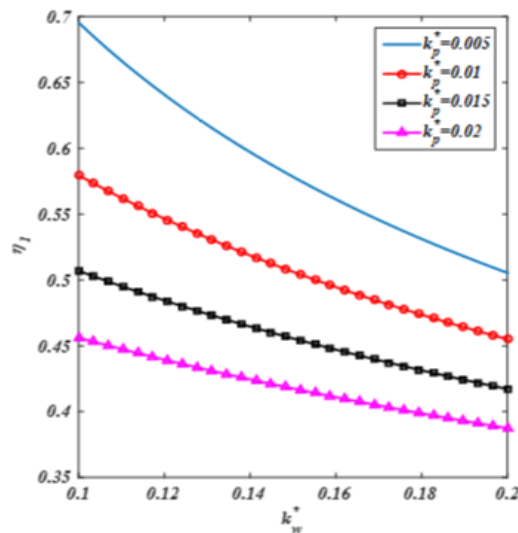
8.5. The Effect of the Winkler and Pasternak Coefficients of the Foundation

Figure 7 (a) investigates the influence of Winkler and Pasternak foundation parameters on the damped natural frequencies and corresponding damping ratios of the beam vibrations (Fig.7 (b)). Increasing the Winkler and Pasternak foundation parameters signifies an enhancement in foundation stiffness. As a result of the interaction between the beam and the foundation, this leads to an elevation in the damped natural frequencies of the beam's vibrations in the first vibration Fig.7 (a) shows that for $k_p^* = 0.02$, Increasing the dimensionless Winkler foundation parameter from 0.1 to 0.2 increases the first-mode ($n=1$) damped natural

frequency of the beam vibrations by about 17%, while the corresponding damping ratio decreases by about 15% (Fig.7 (b)). The figure also shows that for $k_w=0.2$, increasing the dimensionless Pasternak foundation parameter from 0.005 to 0.02 increases the first-mode ($n=1$) damped natural frequency of the beam vibrations by about 29%, while the corresponding damping ratio decreases by about 23%. Mode and a reduction in the corresponding damping ratios, which are observed in Fig. 7.



(a) Resonant Frequencies



(b) Damping Coefficients

Fig. 7. The effect of the winkler coefficient on the natural frequencies and damping coefficients of the beam for various values of the pasternak foundation

9. Conclusions

This study investigated the free vibration of a sandwich beam with an MRE core reinforced with CNTs and GNP-reinforced polymer faces resting on a viscoelastic foundation. The modeling of the core and faces of the beam was based on the

Timoshenko beam theory, and the continuity conditions between the core and face layers were considered. The modeling of the viscoelastic foundation was based on the visco-Pasternak model. The boundary conditions and governing equations were derived using Hamilton's principle, and an exact analytical solution was presented using Navier's method for a sandwich beam under simple (roller) boundary conditions.

- With an increase in the intensity of the magnetic field applied to the core, the damping coefficients of the beam increase in some modes and decrease in others, but overall, the effect of the applied magnetic field intensity on the damping coefficients of the beam is very negligible.
- increasing the mass fraction of CNTs added to the MR core, the resonant frequencies of the beam's vibrations increase.
- With an increase in the thickness of the MR core, the resonant frequencies of the beam's vibrations and the corresponding damping coefficients decrease in all modes of vibration.
- Adding GNPs to the polymer face sheets of the beam is significantly more effective than adding CNTs to its MR core to increase the natural frequencies of the beam.
- Distributing GNPs at a greater distance from the mid-surface of the beam leads to a more significant increase in the natural frequencies of the beam and a greater reduction in the corresponding damping coefficients.
- Increasing the damping coefficient of the foundation results in a decrease in the natural frequencies of the beam in all modes of vibration, while the corresponding damping coefficients increase significantly.

Funding Statement

This research did not receive any specific grant from funding agencies in the public, commercial, or not-for-profit sectors.

Conflicts of Interest

The author declares that there is no conflict of interest regarding the publication of this article.

References

- [1] Akhavan, H., Ehyaei, J. and Ghadiri, M., 2022. Dynamic analysis of magnetorheological elastomer sandwich MEMS sensor under

- magnetic field. *Smart Structures and Systems*, 29(5), pp.705-714.
- [2] Yu, Y., Yousefi, A.M., Yi, K., Li, J., Wang, W. and Zhou, X., 2021. A new hybrid model for MR elastomer device and parameter identification based on improved FOA. *Smart Structures and Systems*, An International Journal, 28(5), pp.617-629.
- [3] Gedik, E., Kurt, H., Recebli, Z. and Balan, C., 2012. Two-dimensional CFD simulation of magnetorheological fluid between two fixed parallel plates applied external magnetic field. *Computers & fluids*, 63, pp.128-134.
- [4] Haghparast, E., Ghorbanpour-Arani, A. and Ghorbanpour Arani A, 2020. Effect of fluid-structure interaction on vibration of moving sandwich plate with Balsa wood core and nanocomposite face sheets. *International Journal of Applied Mechanics*, 12(07), p.2050078.
- [5] Ghorbanpour-Arani, A., Khoddami Maraghi Z and Ghorbanpour Arani A, 2023. The Frequency Response of Intelligent Composite Sandwich Plate Under Biaxial In-Plane Forces. *Journal of Solid Mechanics*, 15(1).
- [6] Zarastvand, M.R., Ghassabi, M. and Talebitooti, R., 2021. A review approach for sound propagation prediction of plate constructions. *Archives of Computational Methods in Engineering*, 28, pp.2817-2843.
- [7] Ghafouri, M., Ghassabi, M., Zarastvand, M.R. and Talebitooti, R., 2022. Sound propagation of three-dimensional sandwich panels: Influence of three-dimensional re-entrant auxetic core. *Aiaa Journal*, 60(11), pp.6374-6384.
- [9] Sun, Y., Zheng, H., Han, Q., and Li, C., 2024. Non-contact electromagnetic controlled metamaterial beams for low-frequency vibration suppression. *International Journal of Solids and Structures*, 290, p.112667.
- [10] Khorshidi, K., Rezaeisaray, M. and Karimi, M., 2022. Energy harvesting using vibrating honeycomb sandwich panels with auxetic core and carbon nanotube-reinforced face sheets. *International Journal of Solids and Structures*, 256, p.111988.
- [11] Ying, Z., Chen, H. and Ni, Y., 2012, April. Magnetorheological visco-elastomer and its application to suppressing micro-vibrations of sandwich plates. In *Third International Conference on Smart Materials and Nanotechnology in Engineering* (Vol. 8409, pp. 356-363). SPIE.
- [12] Joshi, S.B., 2012. Vibration study of magnetorheological fluid-filled sandwich beams. *International Journal of Applied Research in Mechanical Engineering*, 2(2), pp.100-104.
- [13] Aguib, S., Nour, A., Zahloul, H., Bossis, G., Chevalier, Y. and Lançon, P., 2014. Dynamic behavior analysis of a magnetorheological elastomer sandwich plate. *International Journal of Mechanical Sciences*, 87, pp.118-136.
- [14] Nayak, B., Dwivedy, S.K. and Murthy, K.S.R.K., 2014. Dynamic stability of a rotating sandwich beam with magnetorheological elastomer core. *European Journal of Mechanics-A/Solids*, 47, pp.143-155.
- [15] Malekzadeh Fard K., Payganeh, G. and Saghavaz, F.R., 2015. Free vibration and Low-velocity impact Analysis of sandwich plates with Smart Flexible cores. *Modares Mechanical Engineering*, 14(13).
- [16] Ramamoorthy, M., Rajamohan, V. and AK, J., 2016. Vibration analysis of a partially treated laminated composite magnetorheological fluid sandwich plate. *Journal of Vibration and Control*, 22(3), pp.869-895.
- [17] Eshaghi, M., 2020. The effect of magnetorheological fluid and aerodynamic damping on the flutter boundaries of MR fluid sandwich plates in supersonic airflow. *European Journal of Mechanics-A/Solids*, 82, p.103997.
- [18] Eshaghi, M., 2021. Supersonic flutter analysis of annular/circular sandwich panels containing magnetorheological fluid. *Journal of Sandwich Structures & Materials*, 23(7), pp.2968-2987.
- [19] Eshaghi, M., 2023. The optimal core design of MR-based smart panels is subject to flutter instability. *Mechanics Based Design of Structures and Machines*, 51(1), pp.339-358.
- [20] Subramani, M., Ramamoorthy, M., Arumugam, A.B. and Selvaraj, R., 2021. Free and forced vibration characteristics of CNT

- reinforced composite spherical sandwich shell panels with MR elastomer core. *International Journal of Structural Stability and Dynamics*, 21(10), p.2150136.
- [21] Houshang, A., Haghghi, S.E., Jafari, A.A. and Nezami, M., 2022. Free-damped vibration analysis of a truncated sandwich conical shell with a magnetorheological elastomer core. *Waves in Random and Complex Media*, pp.1-28.
- [22] Ghorbanpour Arani A, Eskandari, M. and Haghparast, E., 2022. The supersonic flutter behavior of sandwich plates with a magnetorheological elastomer core and GNP-reinforced face sheets. *International Journal of Applied Mechanics*, 14(09), p.2250015.
- [23] Ghorbanpour Arani A, Shahraki, M.E. and Haghparast, E., 2022. Instability analysis of axially moving sandwich plates with a magnetorheological elastomer core and GNP-reinforced face sheets. *Journal of the Brazilian Society of Mechanical Sciences and Engineering*, 44(4), p.150.
- [24] Selvaraj, R. and Ramamoorthy, M., 2022. Experimental and finite element vibration analysis of CNT reinforced MR elastomer sandwich beam. *Mechanics Based Design of Structures and Machines*, 50(7), pp.2414-2426.
- [25] Selvaraj, R., Subramani, M. and Ramamoorthy, M., 2023. Vibration characteristics and optimal design of composite sandwich beam with partially configured hybrid MR-Elastomers. *Mechanics Based Design of Structures and Machines*, 51(4), pp.2200-2216.
- [26] Arumugam, A.B., Subramani, M., Dalakoti, M., Jindal, P., Selvaraj, R. and Khalife, E., 2023. Dynamic characteristics of laminated composite CNT reinforced MRE cylindrical sandwich shells using HSDT. *Mechanics Based Design of Structures and Machines*, 51(7), pp.4120-4136.
- [27] Selvaraj, R., Ramamoorthy, M. and Arumugam, A.B., 2021. Experimental and numerical studies on the dynamic performance of the rotating composite sandwich panel with CNT-reinforced MR elastomer core. *Composite Structures*, 277, p.114560.
- [28] Khoddami Maraghi, Z., Amir, S. and Arshid, E., 2024. On the natural frequencies of smart circular plates with magnetorheological fluid core embedded between magnetostrictive patches on Kerr elastic substance. *Mechanics Based Design of Structures and Machines*, 52(3), pp.1651-1668.
- [29] Amir, S., Arshid, E., Khoddami Maraghi, Z., Loghman, A. and Ghorbanpour Arani, A., 2020. Vibration analysis of magnetorheological fluid circular sandwich plates with magnetostrictive face sheets exposed to the monotonic magnetic field located on visco-Pasternak substrate. *Journal of Vibration and Control*, 26(17-18), pp.1523-1537.
- [30] Afshari, H. and Adab, N., 2022. Size-dependent buckling and vibration analyses of GNP reinforced microplates based on the quasi-3D sinusoidal shear deformation theory. *Mechanics Based Design of Structures and Machines*, 50(1), pp.184-205.
- [31] Mihankhah, A., Khoddami Maraghi, Z. and Ghorbanpour Arani, A., 2024. Vibration and aeroelastic instability analysis in GPL-porous multi-layered beam with the rotation effect. *International Journal for Computational Methods in Engineering Science and Mechanics*, pp.1-24.
- [32] Soltan Arani, A.H., Ghorbanpour Arani, A. and Khoddami Maraghi Z., 2024. Size-dependent buckling analysis of functionally graded nanoplate coupled with piezoelectric layers resting on an orthotropic foundation based on surface piezo-elasticity theory. *ZAMM-Journal of Applied Mathematics and Mechanics/Zeitschrift für Angewandte Mathematik und Mechanik*, p.e202400425.
- [33] Song, M., Kitipornchai, S. and Yang, J., 2017. Free and forced vibrations of functionally graded polymer composite plates reinforced with graphene nanoplatelets. *Composite Structures*, 159, pp.579-588.
- [34] Ghorbanpour Arani, A., Khoddami Maraghi, Z., Kolahchi, R. and Mohammadimehr, M., 2017. Viscous Fluid Flow-Induced Nonlocal Nonlinear Vibration of Embedded DWBNNTs. *Journal of Solid Mechanics*, 9(4), pp.680-696.

- [35] Khoddami Maraghi, Z., 2019. Flutter and divergence instability of nanocomposite sandwich plate with magnetostrictive face sheets. *Journal of Sound and Vibration*, 457, pp.240-260.
- [36] Soltan Arani, A.H., Ghorbanpour Arani, A. and Khoddami Maraghi, Z., 2024. Nonlocal quasi-3d vibration/analysis of three-layer nanoplate surrounded by Orthotropic Visco-Pasternak foundation by considering surface effects and neutral surface concept. *Mechanics Based Design of Structures and Machines*, pp.1-36.
- [37] Rajamohan, V., Sundararaman, V. and Govindarajan, B., 2013. Finite element vibration analysis of a magnetorheological fluid sandwich beam. *Procedia Engineering*, 64, pp.603-612.